



Defects-engineering of magnetic γ -Fe₂O₃ ultrathin nanosheets/mesoporous black TiO₂ hollow sphere heterojunctions for efficient charge separation and the solar-driven photocatalytic mechanism of tetracycline degradation

Liping Ren, Wei Zhou*, Bojing Sun, Haoze Li, Panzhe Qiao, Yachao Xu, Jiaying Wu, Kuo Lin, Honggang Fu*

Key Laboratory of Functional Inorganic Material Chemistry, Ministry of Education of the People's Republic of China, Heilongjiang University, Harbin 150080, PR China

ARTICLE INFO

Keywords:

Mesoporous black TiO₂ hollow sphere

Heterojunction

Defect

Magnetic separation

Solar-driven photocatalysis

ABSTRACT

Defect-engineered magnetic γ -Fe₂O₃ ultrathin nanosheets/mesoporous black TiO₂ hollow sphere heterojunctions (γ -Fe₂O₃/b-TiO₂) are fabricated by a metal-ion intervened hydrothermal technique and high-temperature hydrogenation, which exhibit wide-spectrum response and magnetic separation. The specific surface area, pore size and pore volume of the resultant γ -Fe₂O₃/b-TiO₂ with hollow structure are $\sim 63 \text{ m}^2 \text{ g}^{-1}$, 10.5 nm and $0.14 \text{ cm}^3 \text{ g}^{-1}$, respectively. After surface hydrogenation, α -Fe₂O₃ nanosheets are converted to γ -Fe₂O₃ ultrathin nanosheets ($\sim 6 \text{ nm}$) combined with the formation of surface defects. The ultrathin nanosheet structure facilitates the surface engineering and also favors the diffusion and transportation of photogenerated charge carriers. The apparent rate constant (k) of defect-engineered γ -Fe₂O₃/b-TiO₂ photocatalytic degradation biotoxic tetracycline is ~ 3 times higher than that of α -Fe₂O₃/b-TiO₂ under AM 1.5 irradiation. The enhancement is attributed to the introduction of narrow bandgap unit-cell-thick γ -Fe₂O₃ nanosheets, the hollow structure and the defect engineering, which are beneficial to solar-light-harvesting and rapid electron transport, and spatial separation of photogenerated charge carriers. The photocatalytic degradation mechanism is also proposed. The novel magnetic γ -Fe₂O₃/b-TiO₂ heterojunction is a promising photocatalyst for recovering the domestic sewage in environment.

1. Introduction

Environmental pollution and energy problems have been two major puzzles for mankind [1,2]. The survival and development of human beings are seriously threatened by the toxic chemical pollution with the development of society. The potential food borne hazards caused by chronic long-term intake of chemical organic pollutants have become a focus of attention, including some carcinogenic and mutagenic processes in the process of pesticide residues, veterinary drug residues, mycotoxins, and food addition [3,4]. Tetracycline is an efficient, widely used antibiotic, an important part of human and veterinary medicine, which can treat a variety of bacterial infections [5,6]. However, antibiotics are a double-edged sword, due to ecological toxicity, lack of biological degradability and the low absorption ability lead to a large number of tetracycline was directly discharged in surface water, groundwater and drinking water [7–9]. The presence of tetracycline in the water results in a huge threat to human health and aquatic ecosystems. Much work so far has focused on the removal technology of

tetracycline, such as biosorption, microbial degradation, electrolysis, photocatalytic oxidation, membrane separation and other removal techniques [10,11]. Due to the lack of biodegradability of antibiotics, the degradation efficiency of antibiotics by biodegradation is very low, and electrocatalysis requires additional electrical energy, which requires huge economic costs. Among them, photocatalytic oxidation technology is considered to be a green, efficient and environmentally friendly alternative to tetracycline wastewater purification.

Since the discovery of TiO₂ photocatalysts by Fujishima in 1972, the photocatalytic oxidation represented by semiconductor photocatalyst has become a promising environmental pollution control technology because of its direct use of solar light driven reaction and good stability of the catalyst [12–14]. It is well known that anatase TiO₂ is a broad band gap semiconductor photocatalyst ($\sim 3.2 \text{ eV}$), absorption of ultraviolet spectrum, low utilization efficiency of visible light and high recombination rate of photo-generated electron-hole still limit its application and development [15,16]. Black TiO₂ can expand absorption to visible light, even near infrared light regions, thereby exhibiting

* Corresponding authors.

E-mail addresses: zwchem@hotmail.com (W. Zhou), fuhg@vip.sina.com, fuhg@hlju.edu.cn (H. Fu).

<https://doi.org/10.1016/j.apcatb.2018.08.033>

Received 11 July 2018; Received in revised form 10 August 2018; Accepted 15 August 2018

Available online 17 August 2018

0926-3373/ © 2018 Published by Elsevier B.V.

excellent photocatalytic properties according to the reports of Mao et al. via hydrogenation, which has been paid widely attention [17]. Although the absorption intensity of black TiO₂ to solar spectrum is obviously improved, because of the existence of a large number of complex centers, it cannot show the expected photocatalytic performance [18–20]. Several excellent reviews described that the construction of the composite semiconductor heterojunctions could effectively inhibit the recombination of photo-generated electrons and holes, thus improving the photocatalytic activity [21–23]. Therefore, black TiO₂ and semiconductor coupling with narrow bandgap, such as Fe₂O₃, not only reduce the recombination of photogenerated electrons and holes, but also can utilize the magnetic separation [24,25].

Hematite nanosheets can achieve the phase transition process by high temperature hydrogenation into magnesite. Due to unique optical, electrical, and physicochemical properties, 2D graphene-like γ -Fe₂O₃ nanosheets-supported semiconductor composite photocatalysts have been widely constructed [26]. However, as a result of the low carrier mobility and minority carrier lifetime short (~ 10 ps), the diffusion length (2–4 nm) and other reasons restrict its application in the field of photocatalysis [27]. According to the previous report that the magnetic Fe₂O₃/black TiO₂ heterojunctions exhibited excellent solar-driven photocatalytic performance and long-term stability. The heterojunctions can better band gap arrangement, so as to improve the separation of photogenerated charge carriers [28].

In this study, we demonstrate a metal-ion intervened hydrothermal technology and high temperature hydrogenation route to prepare the defect-engineered magnetic γ -Fe₂O₃/mesoporous black TiO₂ hollow sphere heterojunctions. The obtained heterojunctions with a unique hollow structure exhibited excellent solar-driven photocatalytic performance and long-term stability for complete decomposition tetracycline. The ultrathin nanosheets structure of γ -Fe₂O₃ favors the separation and transportation of photogenerated charge carriers, which is advantageous of improving the photocatalytic performance. The possible mechanism and degradation pathway of photocatalytic degradation of tetracycline are also proposed. The novel magnetic heterojunctions photocatalysts will become a good choice for domestic sewage treatment in environmental fields.

2. Experimental section

2.1. Chemicals

N, N-Dimethylformamide (DMF), ethylenediamine, triethylamine were of analytical grade and purchased from Tianjin Kemiou Chemical Reagent Co., Ltd. Ferric nitrate (Fe(NO₃)₃·9H₂O), anhydrous oxalic acid and tetrabutyl titanate (TBOT) were analytical grade, aluminum sulfate (Al₂(SO₄)₃) was guaranteed reagent, all purchased from Aladdin Industrial Inc. All chemicals were used as received without further purification. Deionized water was used for all experiments.

2.2. Synthesis

A typical procedure for the synthesis of black TiO₂ hollow spheres was based on previous literature [29]. The γ -Fe₂O₃/b-TiO₂ heterojunctions were obtained by a metal-ion-intervened technique and high-temperature hydrogenation route. Typically, 200 mg black TiO₂ hollow sphere and different amounts of Fe(NO₃)₃·9H₂O were dispersed in 10 mL deionized water followed sonication and stirring for 2 h. Then, a certain amount of aluminum sulfate which according to the ferric nitrate and aluminum sulfate stoichiometric ratio of 4:1 was added to a mixture solution and stirring for 1 h. While fierce stirring, 3 mL of triethylamine was slowly added into the mixture solution and stirring for 30 min. Subsequently, the mixed solution was transferred and sealed in a 50 mL Teflon-lined autoclave. After reactions at 160 °C for 24 h, the resulting red precipitates were filtered, washed three times with deionized water and ethanol, respectively. The obtained mixture was α -

Fe₂O₃/mesoporous black TiO₂ hollow sphere heterojunctions and dried at 60 °C overnight. In order to confirm phase transformation the prepared samples was calcined at 400 °C for 30 min in H₂ with a temperature ramping rate of 10 °C min⁻¹, the obtained α -Fe₂O₃/b-TiO₂ converted to γ -Fe₂O₃/b-TiO₂ heterojunctions. The loaded amounts of Fe₂O₃ were 15, 18, 19, 22 and 24%, respectively, obtained by Inductively Coupled Plasma (Optima 8300 (PerkinElmer, USA) ICP-OES). To prove the effect of the calcination temperature of hydrogenation, different calcination temperatures of 300, 350, 400, 450, 500 °C, respectively, were performed. In parallel, the samples synthesized without hydrogenation was also prepared for comparison.

2.3. Characterizations

Powder X-ray diffraction (XRD) patterns were analyzed by a Bruker D8 Advance diffractometer with monochromatized Cu K α radiation ($\lambda = 1.5406$ Å, with the accelerating voltage of 40 kV and the applied current of 20 mA). The refinement structure and morphology of the samples were recorded on scanning electron microscopy (SEM, FEI Sirion 200 instrument operated at 15 kV) and transmission electron microscopy (TEM, Tecnai G2 F20), with an acceleration voltage of 200 kV). The X-ray photoelectron spectroscopy (XPS) measurements were performed to investigate the surface states on a ULTRAAXIS DLD with an Al K α (1253.6 eV) achromatic X-ray source by referencing to the C 1s peak at 284.6 eV. The diffuse reflectance spectroscopy (DRS) was carried out on a UV-vis spectrophotometer (Lambda 950 (PerkinElmer, USA)) in the range of 200–1800 nm, with fine BaSO₄ powders as reference. Nitrogen adsorption-desorption isotherms at 77 K were collected on an AUTOSORB-1 (Quantachrome Instruments) nitrogen adsorption apparatus. The Brunauer-Emmett-Teller (BET) equation was used to estimate the specific surface area. Pore size distributions were measured using the Barrett-Joyner-Halenda (BJH) measurements from the adsorption branch of the isotherms. The total organic carbon (TOC) removal was tested on the TOC analysis equipped with analytic jena multi NIC 2100 analyzer. The magnetic hysteresis loops were obtained by a LakeShore 7404 (LakeShore, USA) vibrating sample magnetometer (VSM).

2.4. Photocatalytic activity measurements

The photocatalytic activity was tested by the photocatalytic degradation of tetracycline (C₂₂H₂₄N₂O₈). AM 1.5 solar power system was used as the light irradiation source, equipped with 300 W Xe lamp (with an AM 1.5 filter) and calibrated the optical intensity was 100 mW cm⁻² before performance. Typically, the as-prepared photocatalyst (30 mg) was added to 100 mL tetracycline solution (10 mg L⁻¹). In order to reach adsorption-desorption equilibrium, the suspensions were stirred in the dark for 10 min before irradiation at room temperature. Then, the suspense was radiated under intense agitation, took 8 mL solution once per 10 min and filtered through 0.22 μ m Millipore filters to reject the catalysts. The residue tetracycline and its degradation products were detected by LC-MS, which equipped with Bruker micrOTOF-Q mass spectrometer coupled to an Agilent 1200 series HPLC with EC C18 reverse-phase column (50 \times 2.1 mm, 1.7 μ m particle, Agilent) at 25 °C and UV detector. The detection wavelength of the UV detector was 355 nm and the injection volume was 2 μ L. The isocratic mobile phase was made up of 20% acetonitrile and 80% water (with 0.1% formic acid) with a flow rate of 0.3 mL min⁻¹. The mass spectrometer analysis was operated in positive ionization mode over the range of m/z 100–600 with an electrospray ionization (ESI) source. Nitrogen (99.99% purity) was used as the dissolving gas with a flow rate at 4 L min⁻¹. In order to confirm the stability of the photocatalysts, the catalysts were recycled after experiments and cleaned several times by deionized water and ethanol, and then drying at 60 °C for 12 h to remove the residual reactants and reactivate the adsorption and catalytic performance.

2.5. Photoelectrochemical measurements

Photoelectrochemical properties were analyzed by Princeton Versa STAT 3electrochemical station in a three-electrode system with Ag/AgCl as reference, Pt plate as counter electrode, α -Fe₂O₃/b-TiO₂ and γ -Fe₂O₃/b-TiO₂ materials used as photoanodes in home-built crystal, 1 M KOH aqueous solution was used as an electrolyte. The test conditions for electrochemistry are as follows, AC properties was set up start frequency 10,000 Hz and end frequency 0.1 Hz, scan properties was controlled 30 point per decade and DC potential was vs OC with over-voltage was 600 mV. The preparation of photoanodes were by a traditional spray coating method, using a transparent FTO glass-substrate (TCO, fluorine doped SnO₂ layer, Nippon sheet glass, Japan) to roll a paste containing 0.1 g of powders without hydrogenation and 2 mL of EtOH, followed by calcining for 2 h at 350 °C under a N₂ atmosphere with a constant heating rate of 5 °C min⁻¹, then annealing at 400 °C for 30 min in H₂ with a temperature ramping rate of 10 °C min⁻¹. 1 M KOH purged with N₂ was used as the electrolyte. An AM 1.5 power system (Oriel, USA) was used as the light irradiation source.

3. Results and discussion

3.1. Crystal structure and morphology of γ -Fe₂O₃/b-TiO₂ heterojunctions

In this study, we firstly investigated a metal-ion-intervened technique hydrothermal method to prepare α -Fe₂O₃ graphene-like nanosheets/b-TiO₂ heterojunctions. Then the α -Fe₂O₃ nanosheets can be converted to γ -Fe₂O₃ by a subsequent phase transition process while preserving the graphene-like 2D morphology due to crystal lattice matching [30]. According to literatures, hematite was used as precursor to prepare magnetic magnetite by reduction and reoxidation [31,32]. Compared with the previous phase transformation mode of reduction and reoxidation, a mild reduction method may be safer and directly achieve the phase transformation method. The suitable temperature of hydrogenation can achieve the above phase transformation. The crystal structure of the γ -Fe₂O₃/b-TiO₂ heterojunctions annealing hydrogenation at 400 °C and α -Fe₂O₃/b-TiO₂ heterojunctions without hydrogenation are analyzed by X-ray diffraction as shown in Fig. 1A. It clearly shows five typical crystal peaks at $2\theta = 25.2, 37.8, 48.1, 53.9$ and 55.1° , which could be indexed as anatase TiO₂ (JCPDS no. 21-1272). The remaining diffraction peaks can be indexed to the hexagonal phase α -Fe₂O₃ (JCPDS no. 33-0664) and magnetite γ -Fe₂O₃ (JCPDS no. 39-1436), respectively [33]. The result proves the effective coupling between Fe₂O₃ and TiO₂. The UV–vis absorption spectra of α -Fe₂O₃/b-TiO₂ and γ -Fe₂O₃/b-TiO₂ heterojunctions are shown in Fig. 1B. For both α -Fe₂O₃/b-TiO₂ and γ -Fe₂O₃/b-TiO₂ heterojunctions, a sharp increase in absorption at wavelengths shorter than 400 nm can be ascribed to the intrinsic absorption of crystalline anatase TiO₂. The absorption from UV to near infrared region (up to 1800 nm) may be contributed to the coupling of narrow band gap semiconductors with visible light response for Fe₂O₃. However, the γ -Fe₂O₃/b-TiO₂ heterojunctions exhibit stronger absorption in the visible-light and infrared region than that of the α -Fe₂O₃/b-TiO₂ heterojunctions, attributable to the formation of more oxygen vacancies under the more appropriate hydrogenation temperature condition than the latter [34]. Fig. 1C and D show N₂ adsorption-desorption isotherms and the corresponding pore-size distribution curves of α -Fe₂O₃/b-TiO₂ and γ -Fe₂O₃/b-TiO₂ heterojunctions, respectively. Both curves show typical type-IV hysteresis loop, indicating the mesoporous material. The Brunauer–Emmett–Teller surface area and pore size subtle vary after hydrogenation, in which the surface area, pore size and pore volume for α -Fe₂O₃/b-TiO₂ heterojunctions are $\sim 60 \text{ m}^2 \text{ g}^{-1}$, 11.0 nm and $0.14 \text{ cm}^3 \text{ g}^{-1}$, and γ -Fe₂O₃/b-TiO₂ heterojunctions are $\sim 63 \text{ m}^2 \text{ g}^{-1}$, 10.5 nm and $0.14 \text{ cm}^3 \text{ g}^{-1}$, respectively. This variation can be attributed to the formation a layer of disorders on the surface of Fe₂O₃ nanosheets, which is in good

agreement with the literature [29]. The specific surface area of the obtained heterojunction samples was much smaller than that of the pure hollow spheres (Fig. S1), implying the efficient loading of Fe₂O₃ nanosheets.

The morphology and microstructure after H₂ annealing treatment of γ -Fe₂O₃/b-TiO₂ are studied by scanning electron microscope (SEM) and transmission electron microscopy (TEM) techniques. As can be seen from the SEM image (Fig. 2A), the uniform γ -Fe₂O₃ nanosheets grow firmly on the surface of the black TiO₂ hollow sphere with a diameter of ~ 700 nm. The thickness of γ -Fe₂O₃ ultrathin nanosheets is ~ 6 nm, which are obtained by atomic force microscope (AFM) as shown in the Fig. S2. TEM image further demonstrates the microstructure of γ -Fe₂O₃ nanosheets/TiO₂ hollow sphere heterojunctions (Fig. 2B). The special nanostructures could be favorable for light absorption and the rapid transfer of electrons and holes, resulting in good photocatalytic performance [35]. In addition, the high-resolution transmission electron microscopy (HRTEM) image in Fig. 2C show both the γ -Fe₂O₃ nanosheets combined in hollow sphere heterojunctions, and exhibits clear lattice fringes with interplane distances of 0.35 and 0.30 nm could be observed obviously, corresponding to the anatase TiO₂ (101) and γ -Fe₂O₃ crystallographic planes (311), respectively [36]. The energy dispersive X-ray (EDS) elemental mappings (Fig. 2D–G) confirm that the Ti, Fe, and O are uniformly distributed in γ -Fe₂O₃/b-TiO₂ heterojunctions, further indicating that the γ -Fe₂O₃ is united in wedlock on mesoporous black TiO₂ hollow spheres.

The X-ray photoelectron spectra (XPS) could reveal the chemical state of the resultant heterojunctions. Fig. 3A shows survey spectrum of γ -Fe₂O₃/b-TiO₂, the Ti, Fe, C and O peaks are present in the γ -Fe₂O₃/b-TiO₂ heterojunctions. The XPS peaks of Fe 2p_{3/2} and Fe 2p_{1/2} for the α -Fe₂O₃/b-TiO₂ and γ -Fe₂O₃/b-TiO₂ heterojunctions are shown in Fig. 3B. It clearly indicates that the two main peaks of Fe after hydrogenation are shifted to a high binding energy direction. The position of Fe 2p_{3/2} and Fe 2p_{1/2} are located at ~ 710.9 and 724.7 eV. A distinct satellite peak at 718.5 eV is assigned to γ -Fe₂O₃, which are similar to literatures [36,37]. As shown in Fig. 3C, the Ti 2p XPS spectra of γ -Fe₂O₃/b-TiO₂ heterojunctions show a slightly shift towards lower binding energy, which indicates the variety in chemical environment of Ti atoms. There are four peaks at 464.17, 463.35, 459.48 and 458.11 eV, attributing to Ti⁴⁺ 2p_{1/2}, Ti³⁺ 2p_{1/2}, Ti⁴⁺ 2p_{3/2} and Ti³⁺ 2p_{3/2}, respectively. This clearly shows the presence of Ti³⁺, in good agreement with literatures [38,39]. The O 1s XPS spectra of γ -Fe₂O₃/b-TiO₂ heterojunctions is presented in Fig. 3D. Four peaks at 532.9, 531.4, 530.5 and 529.4 eV are the characteristic signals of the hydroxyl oxygen, oxygen vacancy surface adsorbed oxygen and lattice oxygen, respectively [40]. It is generally accepted that the formation of oxygen vacancies conduces to the generation of unpaired electrons or Ti³⁺ centers and facilitates the charge separation at the semiconductor-electrolyte interface, which attributable to the increasing of donor levels in the electronic structure of metal oxide. In addition, the existence of oxygen vacancies affects the recombination efficiency of photogenerated electron-hole pairs and prolongs the lifetime of carriers, thereby improving the photocatalytic performance [41,42].

3.2. Photocatalytic activity and mechanism

The photocatalytic performance of γ -Fe₂O₃/b-TiO₂ heterojunctions has been evaluated preliminarily by degrading the tetracycline solution under AM 1.5 irradiation. As can be seen from Fig. 4A, the photocatalytic degradation performance of tetracycline can be up to 99.3% with 50 min, which is much higher than that of α -Fe₂O₃/TiO₂ heterojunctions. The linear relation of $-\ln(\text{TOC}/\text{TOC}_0)$ for γ -Fe₂O₃/b-TiO₂ and α -Fe₂O₃/b-TiO₂ heterojunctions can be obtained and the linear trend demonstrates that the photocatalytic behaviors of tetracycline under these reaction conditions are well fitted with pseudo-first-order. In addition, the γ -Fe₂O₃/b-TiO₂ exhibits the highest photocatalytic degraded rate constant ($k = 0.0829 \text{ min}^{-1}$), which is about 3 times higher

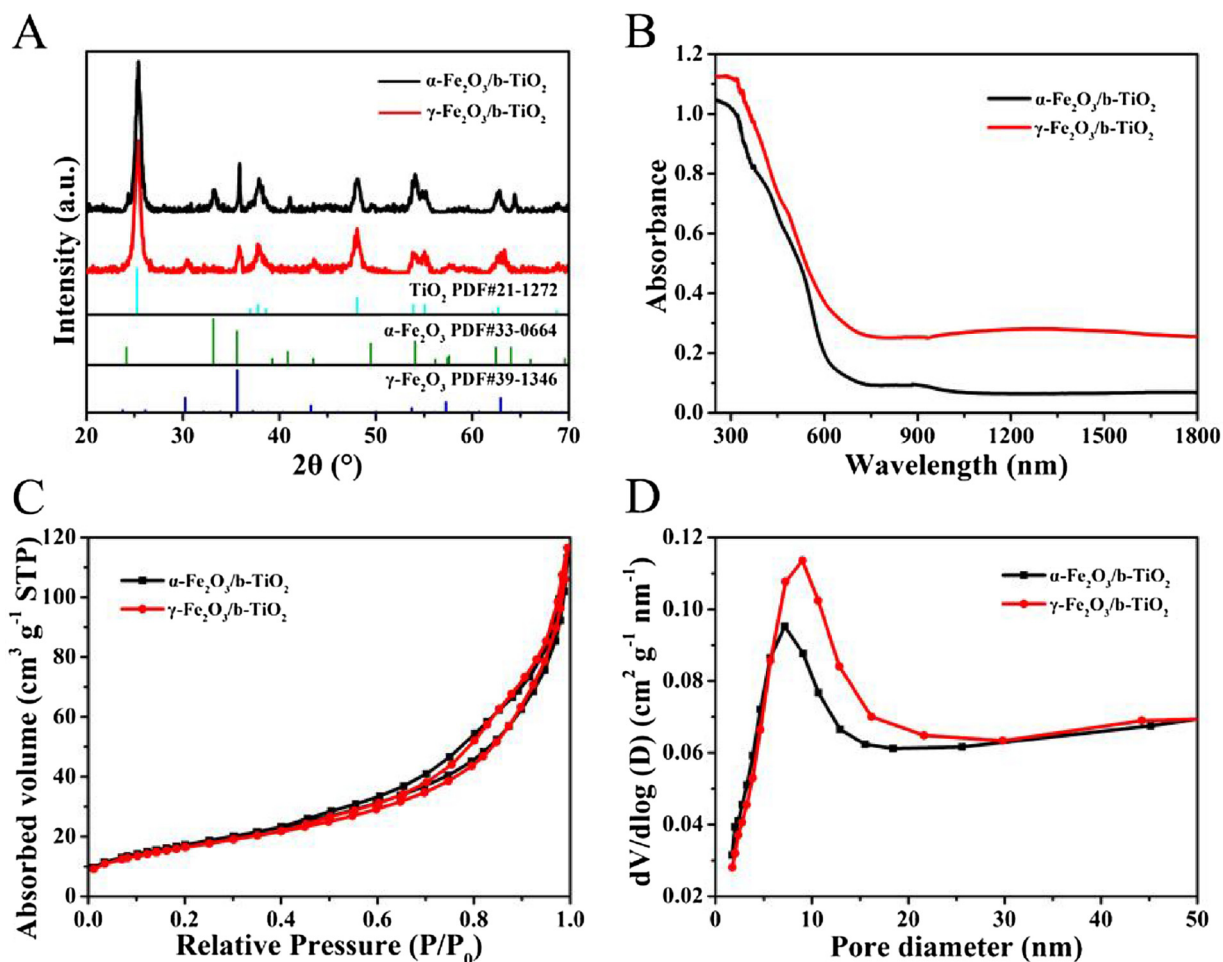


Fig. 1. Typical XRD patterns (A), UV–vis spectra (B), N_2 adsorption-desorption isotherms (C) and the corresponding BJH pore size distribution plots (D) of $\alpha\text{-Fe}_2\text{O}_3/\text{b-TiO}_2$ and $\gamma\text{-Fe}_2\text{O}_3/\text{b-TiO}_2$, respectively.

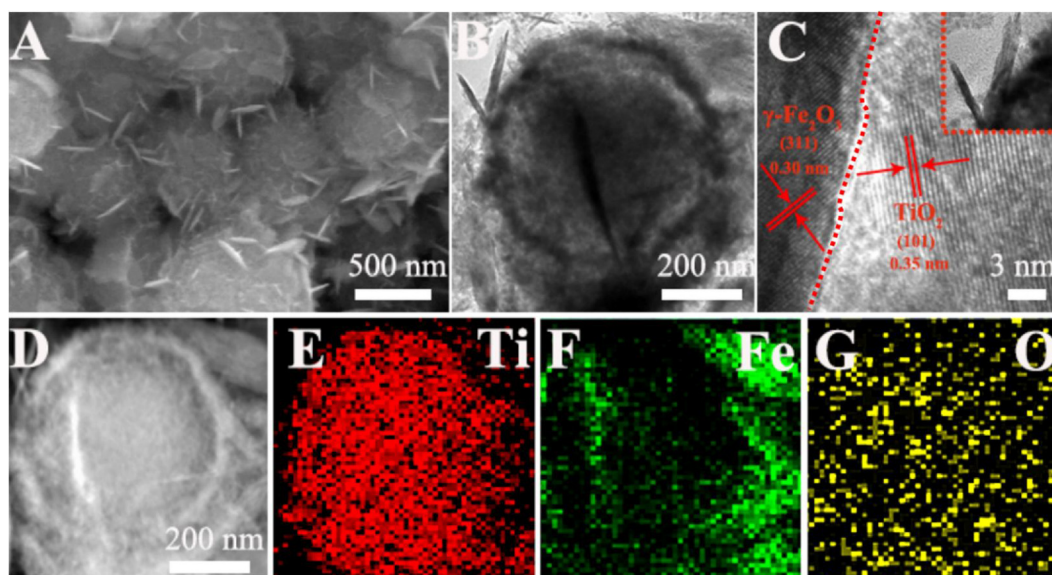


Fig. 2. The SEM (A), TEM (B), HRTEM image (C) and EDS elemental mappings (D–G) of $\gamma\text{-Fe}_2\text{O}_3/\text{b-TiO}_2$ heterojunctions.

than that of the pristine $\alpha\text{-Fe}_2\text{O}_3/\text{TiO}_2$ (0.0281 min^{-1}). The high photocatalytic performance of $\gamma\text{-Fe}_2\text{O}_3/\text{b-TiO}_2$ heterojunctions could be ascribed to the narrow bandgap extending the photoresponse to visible-light and near infrared regions, and the disordered layer caused by the

self-doping of Ti^{3+} , more surface active centers are produced, which promotes the separation of the photogenerated electron-hole pairs and accelerates the electron transfer. Another nonnegligible reason is the introduction of ultrathin $\gamma\text{-Fe}_2\text{O}_3$ nanosheets with unique thin

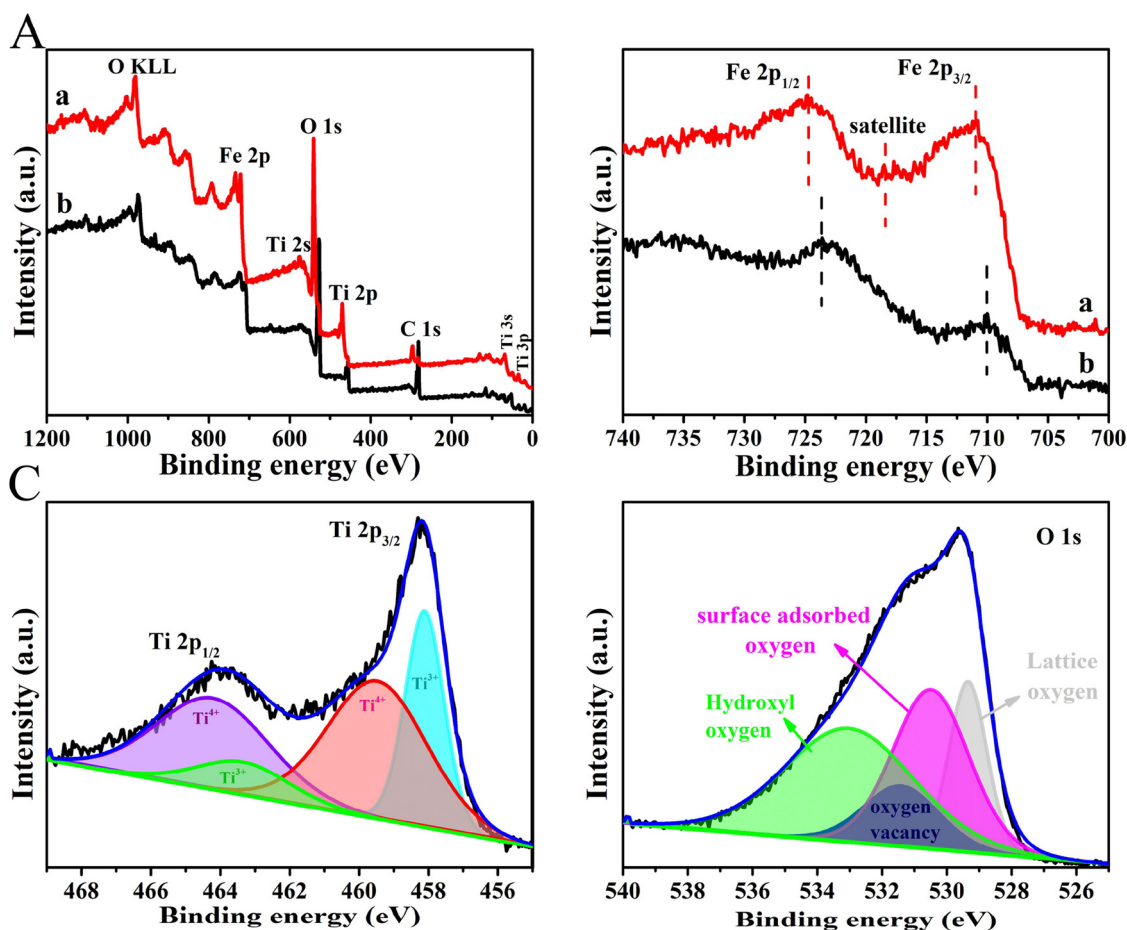


Fig. 3. XPS spectra of the full survey spectra (A), Ti 2p (C) and O 1s (D) of γ -Fe₂O₃/b-TiO₂ heterojunctions, Fe 2p (B) of γ -Fe₂O₃/b-TiO₂ (a) and α -Fe₂O₃/b-TiO₂ (b), respectively.

thickness. This two-dimensional structure could expose the most effective active sites and shorten the diffusion distance of charge carriers, which are responsible for the excellent photocatalytic performance. Furthermore, the heterojunction between γ -Fe₂O₃ nanosheets and black TiO₂ hollow spheres can promote the separation of photogenerated electron-hole pairs due to the formation of efficient heterojunctions. The efficient separation of photogenerated electron-hole pairs of the γ -Fe₂O₃/b-TiO₂ heterojunctions is further demonstrated by the surface photovoltage spectroscopy (SPS) analysis (Fig. S3A). Compared to α -Fe₂O₃/b-TiO₂ heterojunctions, the onset of the γ -Fe₂O₃/b-TiO₂ heterojunctions is red-shifted, suggesting the visible light photoactive. Moreover, after the high temperature hydrogenation, the lifetime of photogenerated charges is greatly prolonged according to transient-state fluorescence spectra (Fig. S3B), which further offers evidence for the high photocatalytic performance of the γ -Fe₂O₃/TiO₂ heterojunctions. The photocatalytic degradation performance of tetracycline for γ -Fe₂O₃/b-TiO₂ heterojunctions with different loading amounts of γ -Fe₂O₃ are shown in Fig. 4B. It is worthwhile mentioning that the photocatalytic degradation ratios of tetracycline are increased firstly and then decreased. The results suggested that when the loading capacity of γ -Fe₂O₃ is 22%, it shows the outstanding property.

To deeply explore the boosting solar-driven photocatalytic performance of γ -Fe₂O₃/b-TiO₂ heterojunctions, the performances of single wavelength with 365, 420, 520 and 950 nm are tested as Fig. S4. Under the same light intensity, the b-TiO₂ and γ -Fe₂O₃/b-TiO₂ heterojunctions under ultraviolet light (under 365 nm irradiation) have the best photocatalytic degradation performance of tetracycline compared with other single wavelengths, it proved that both of them are able to use ultraviolet light efficiently. The photocatalytic degradation rates under

irradiation of 420 and 520 nm are similar and lower than the degradation rate of 365 nm. It is obvious that the performance of the γ -Fe₂O₃/b-TiO₂ heterojunctions is better than that of b-TiO₂. The γ -Fe₂O₃/b-TiO₂ heterostructure also has excellent photocatalytic properties in the near infrared region with the wavelength under 950 nm irradiation. And the photocatalytic degradation of the γ -Fe₂O₃/b-TiO₂ heterojunction is about 2.5 times as high as that of the b-TiO₂, confirming that the thermal effect of near infrared light promotes the process of photocatalytic oxidation. In order to further investigate thoroughly the role of heterojunction, under the condition of the load amount of γ -Fe₂O₃ was 22%, several comparison experiments were carried out on the performance test as can be seen from Fig. S5. Compared with b-TiO₂, α -Fe₂O₃/b-TiO₂ heterojunctions, γ -Fe₂O₃/b-TiO₂ heterojunctions, γ -Fe₂O₃&b-TiO₂ (the physical mixture of mesoporous black TiO₂ hollow spheres and γ -Fe₂O₃ nanosheet, referred to as γ -Fe₂O₃&b-TiO₂, with a weight ratio of 7:13) and γ -Fe₂O₃/b-TiO₂ after being crushed, γ -Fe₂O₃/b-TiO₂ heterojunctions shows the best photocatalytic performance. And their *k* values are shown in Table S1. The results show that the two phases physical mixing cannot improve the photocatalytic performance, which is attributable to poor contact and hinders the migration of the carrier. It further confirms that the heterojunction can effectively promote the separation of electrons and holes. The presence of γ -Fe₂O₃ nanosheets can improve the absorption efficiency of the material to the sunlight, and meanwhile its vertical growth on surfaces of mesoporous black TiO₂ hollow spheres cannot obstruct the capture of light by TiO₂. Therefore, the heterojunction structure made of ultra-thin γ -Fe₂O₃ nanosheets and mesoporous black TiO₂ hollow spheres will become excellent optical traps. From the results we also have obtained that after being crushed, the photocatalytic

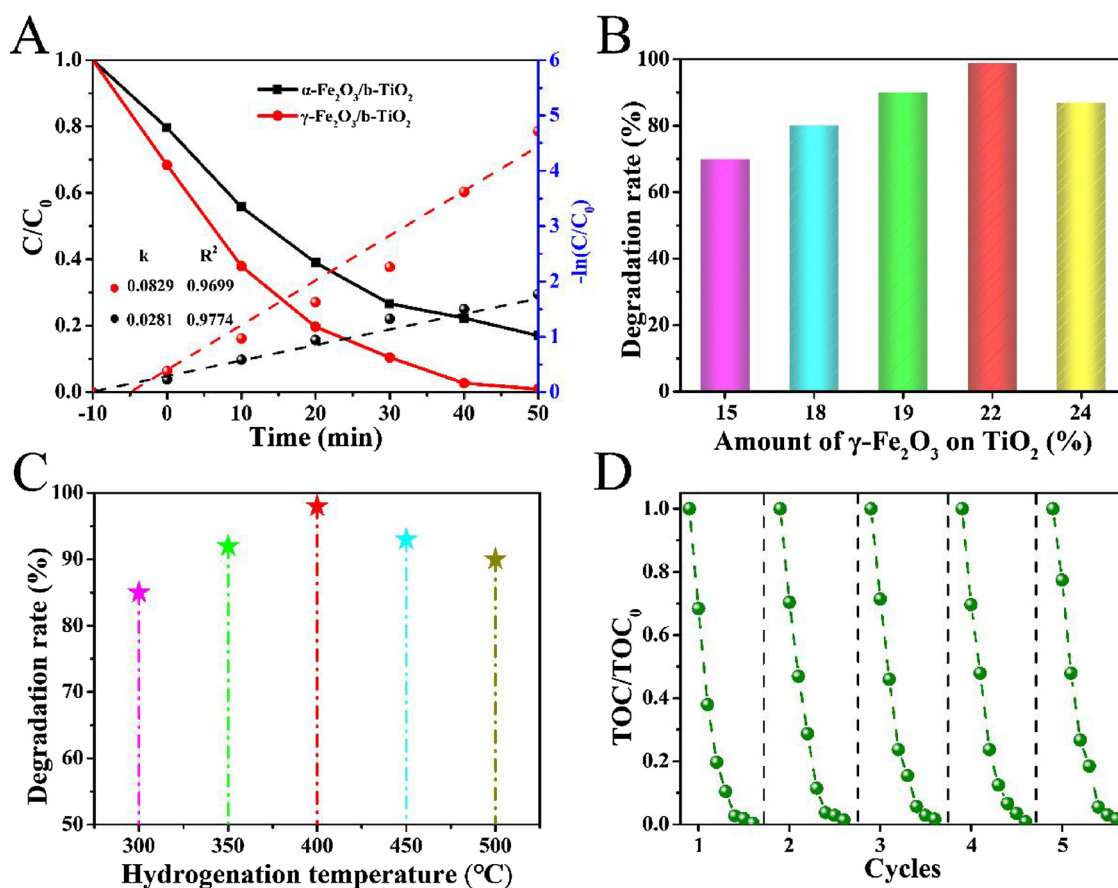


Fig. 4. Photocatalytic degradation performances of tetracycline and the corresponding variations in $-\ln(\text{TOC}/\text{TOC}_0)$ of $\gamma\text{-Fe}_2\text{O}_3/\text{TiO}_2$ and $\gamma\text{-Fe}_2\text{O}_3/\text{b-TiO}_2$ heterojunctions under AM 1.5 irradiation (A). Photocatalytic degradation tetracycline performance of $\gamma\text{-Fe}_2\text{O}_3/\text{b-TiO}_2$ heterojunctions with different loading amounts of $\gamma\text{-Fe}_2\text{O}_3$ (B) and different hydrogenation temperature (C), the recycle of $\gamma\text{-Fe}_2\text{O}_3/\text{b-TiO}_2$ heterojunctions for tetracycline photodegradation (D).

properties of the heterojunction decreased obviously, it may be due to the destruction of the hollow sphere structure by ball milling. As a result of that the hollow sphere structure has the advantage of multiple refraction of incident light, thus enhancing the light utilization.

In order to explore the effect of different hydrogenating temperature on the photocatalytic performance, the samples (the load amount of $\gamma\text{-Fe}_2\text{O}_3$ is 22%) are treated at different hydrogenated temperatures and compared as shown in Fig. 4C. With the increase of hydrogenation temperature, the degradation rate of tetracycline increased first and then decreased. It is well known that hydrogen treatment can produce oxygen defects, which can be electron donors and improve charge transport. Nevertheless, when the concentration of defects is too high, they will become the recombination center of electrons and holes, which will reduce the photocatalytic performance [43,44]. The hematite nanosheets can be converted to maghemite through hydrogenated treatment, while preserving the graphene like 2D morphology due to crystal lattice matching by a subsequent phase transition process.

The magnetic properties could favor the separation and recycle of $\gamma\text{-Fe}_2\text{O}_3/\text{b-TiO}_2$ catalyst from the aqueous solution by an external magnetic field as seen in Fig. S6. After the magnetic separation and recovery of the samples, the original stability and photocatalytic activity can be effectively maintained. The recycling performance test of the recovered samples is shown in Fig. 4D. After 5 cycles of magnetic separation samples, the photocatalytic properties of tetracycline for $\gamma\text{-Fe}_2\text{O}_3/\text{b-TiO}_2$ heterojunctions remained constant. After storing for six months, it is consistent with the observation from the fresh one Fig. S7, further illustrating that the magnetic $\gamma\text{-Fe}_2\text{O}_3/\text{b-TiO}_2$ heterojunction is highly stable and has great practical application value in the environment.

Hydroxylradical ($\cdot\text{OH}$) is the most important oxidative active species in photocatalytic reactions and play a crucial role in the decomposition of organic molecules. Coumarin was chosen as a fluorescence probe because it could react with $\cdot\text{OH}$ in basic solution to generate 7-hydroxycoumarin, in which the fluorescence signal is at around 470 nm [45,46]. Significant fluorescence spectra can be observed under AM 1.5 irradiation from Fig. 5A. The fluorescence intensity is enhanced with the increase of irradiation time. The linear relationship between fluorescence intensity and irradiation time (the inset of Fig. 5A) confirms the stability of $\gamma\text{-Fe}_2\text{O}_3/\text{b-TiO}_2$ heterojunctions. Interestingly, the $\cdot\text{OH}$ density of $\gamma\text{-Fe}_2\text{O}_3/\text{b-TiO}_2$ heterojunction is much higher than that of $\alpha\text{-Fe}_2\text{O}_3/\text{b-TiO}_2$ heterojunction, resulting in the high photocatalytic performance for the former. The magnetic properties of $\alpha\text{-Fe}_2\text{O}_3/\text{b-TiO}_2$ and $\gamma\text{-Fe}_2\text{O}_3/\text{b-TiO}_2$ heterojunctions were tested by the vibrating sample magnetometer (VSM) as shown in Fig. 5B. The magnetic saturation (M_s) values of the $\alpha\text{-Fe}_2\text{O}_3/\text{b-TiO}_2$ and $\gamma\text{-Fe}_2\text{O}_3/\text{b-TiO}_2$ heterojunctions are 0.68 and 8.17 emu/g, respectively. According to reports, the magnetization for $\gamma\text{-Fe}_2\text{O}_3/\text{b-TiO}_2$ heterojunctions can reach the requirements of magnetic separation [47]. Therefore, fabricating magnetic composite material provides a more impactful way for the recycle of photocatalysts, and effectively solves the general slurry TiO_2 catalyst system to recycle.

Electrochemical impedance spectroscopy (EIS) was carried out to investigate the interface charge separation efficiency for the resultants under dark and AM 1.5 irradiation (Fig. 5C). The electrochemical impedance spectroscopy shows the smaller interfacial resistance for $\gamma\text{-Fe}_2\text{O}_3/\text{b-TiO}_2$ than that of $\alpha\text{-Fe}_2\text{O}_3/\text{b-TiO}_2$ heterojunctions, suggesting the efficient charge separation by reducing the recombination of electron-hole pairs for $\gamma\text{-Fe}_2\text{O}_3/\text{b-TiO}_2$ heterojunctions. From the Fig. 5D,

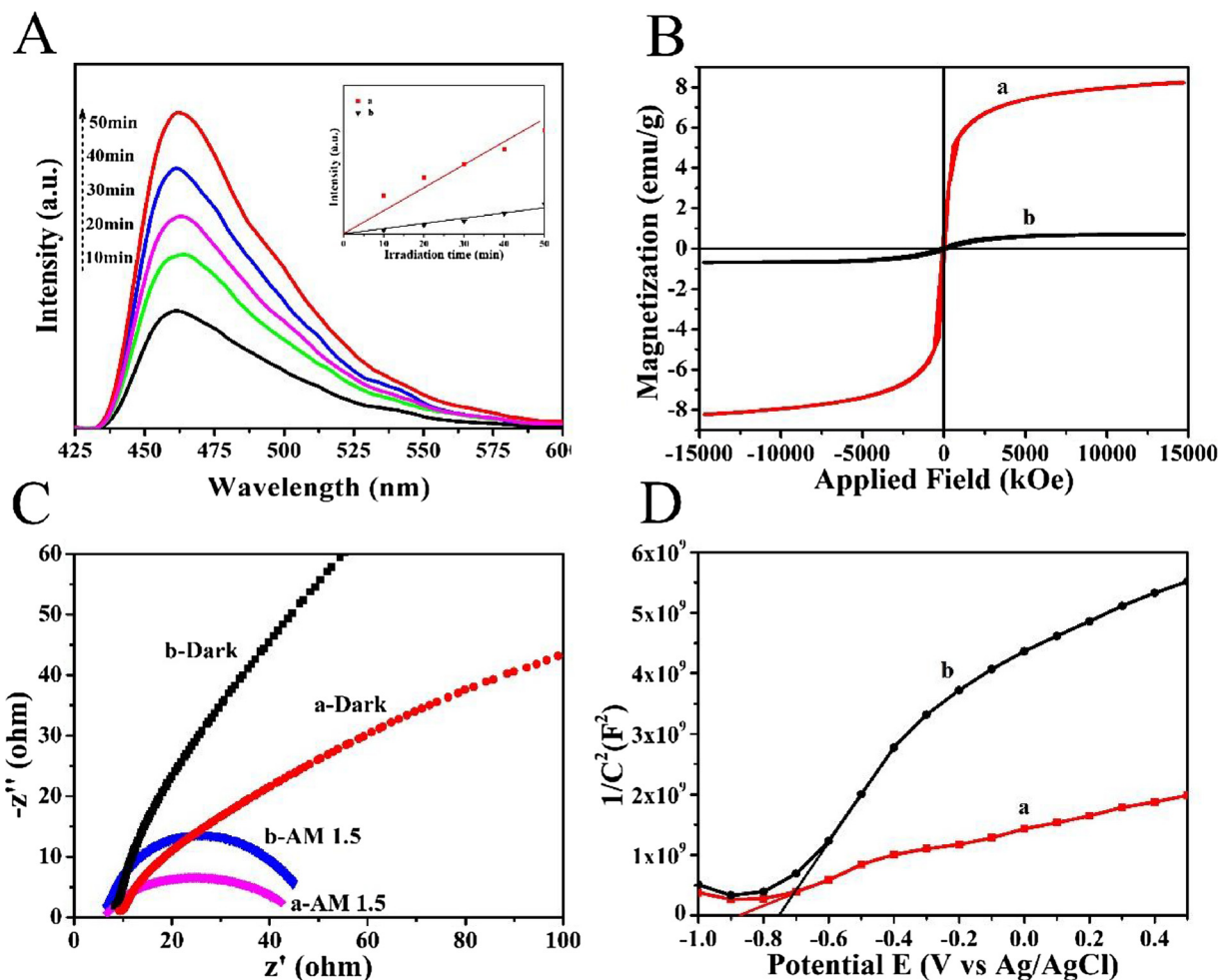


Fig. 5. Fluorescence spectra (A) of $\gamma\text{-Fe}_2\text{O}_3/\text{b-TiO}_2$ heterojunctions under AM 1.5 irradiation. The inset depicts the time dependences of fluorescence intensity at 470 nm. Magnetization hysteresis loops (B), Nyquist plots (C) of electrochemical impedance in the dark and under AM 1.5, and Mott-Schottky plots (D) of $\gamma\text{-Fe}_2\text{O}_3/\text{b-TiO}_2$ heterojunctions (a) and $\alpha\text{-Fe}_2\text{O}_3/\text{b-TiO}_2$ (b), respectively.

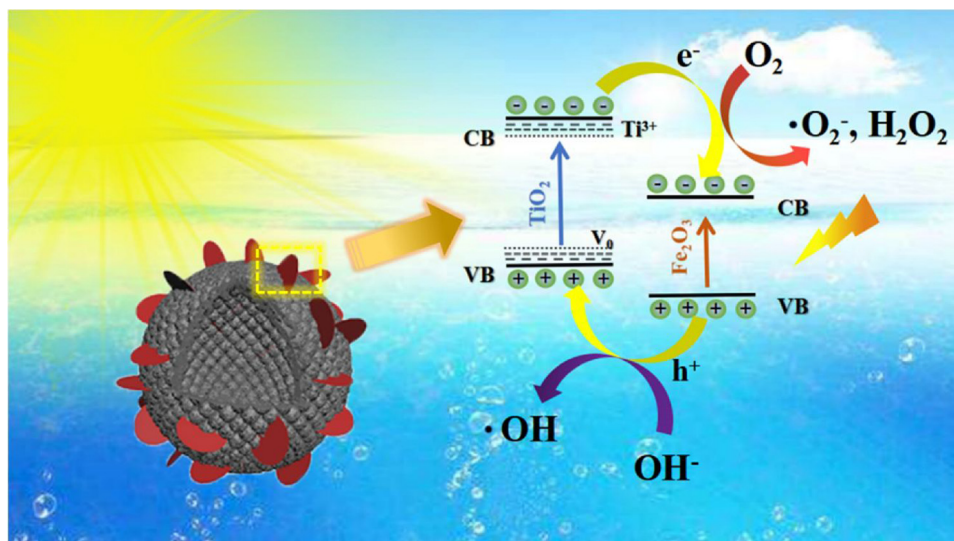
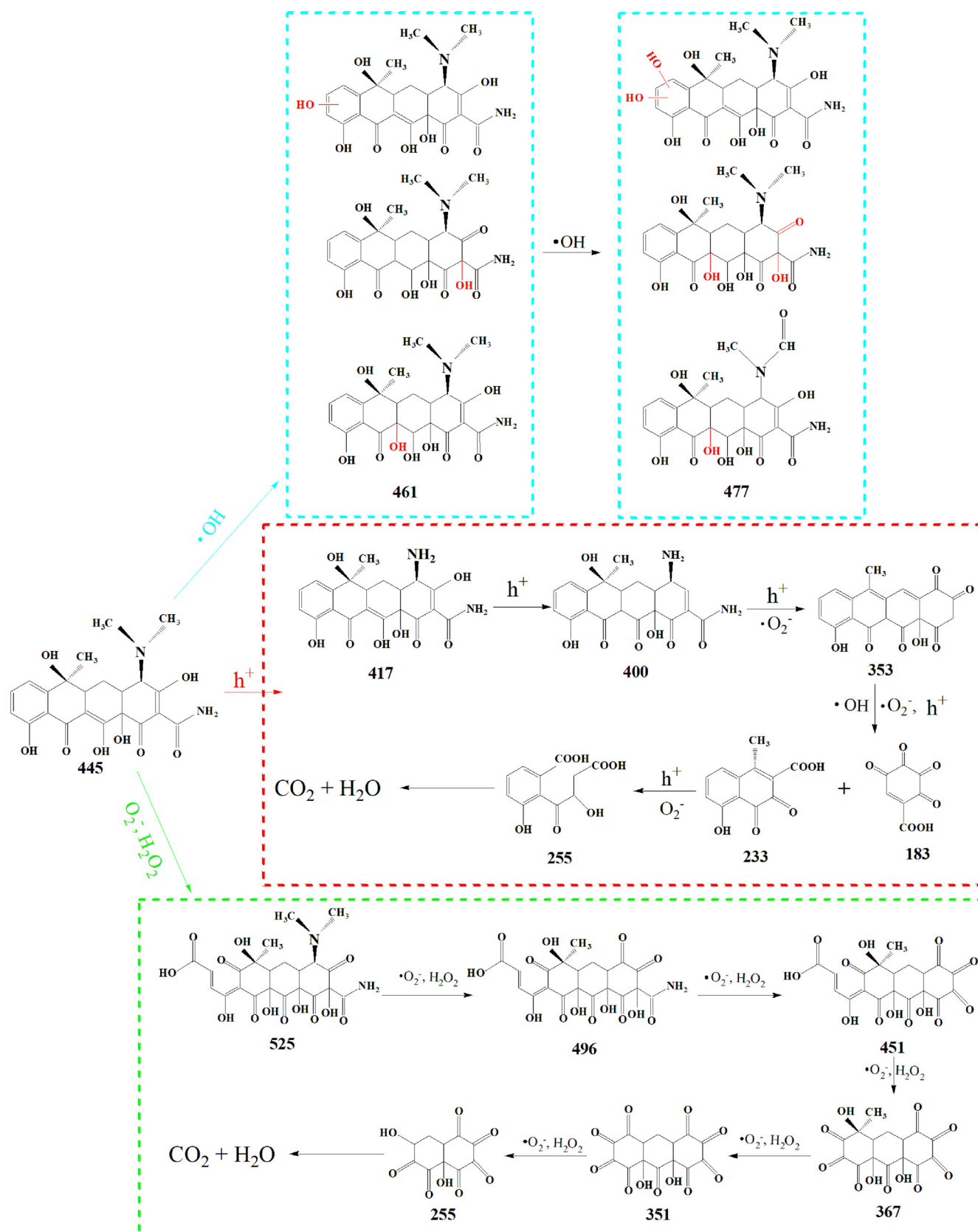


Fig. 6. Schematic illustration of the energy band structure for $\gamma\text{-Fe}_2\text{O}_3/\text{b-TiO}_2$ heterojunctions and the proposed photogenerated charge transfer mechanism.

we can see that $\gamma\text{-Fe}_2\text{O}_3/\text{b-TiO}_2$ and $\alpha\text{-Fe}_2\text{O}_3/\text{b-TiO}_2$ heterojunctions exhibit a positive slope in the Mott-Schottky plots, which is direct evidence of n-type semiconductor behavior for both of them. Furthermore, a shallower slope for $\gamma\text{-Fe}_2\text{O}_3/\text{b-TiO}_2$ could be obtained

compared to $\alpha\text{-Fe}_2\text{O}_3/\text{b-TiO}_2$ heterojunctions, suggesting an increase of donor density after hydrogenation. The carrier density could be calculated from the corresponding slope according to Eq. (1).



Scheme 1. The proposed structures of intermediates and the suggest transformation pathways of photocatalytic tetracycline degradation. (For interpretation of the references to colour in the text, the reader is referred to the web version of this article.)

$$N_d = \frac{2/\epsilon_0\epsilon\epsilon_0}{d(1/C^2)/dv} \quad (1)$$

We take $\epsilon = 55$ for anatase TiO_2 [48]. The electron densities of $\gamma\text{-Fe}_2\text{O}_3/\text{b-TiO}_2$ and $\alpha\text{-Fe}_2\text{O}_3/\text{b-TiO}_2$ heterojunctions are approximately 2.1×10^{19} and $0.4 \times 10^{19} \text{ cm}^{-3}$, respectively. The increased carrier density is ascribed to the presence of Ti^{3+} , oxygen vacancy defects, ultrathin nanosheet structure and the successful construction of heterojunction gives rise to better electron-hole pair separation and transport. That would be responsible for improving the photocatalytic performance.

According to experimental results and the XPS valence-band spectra, the corresponding band structures of $\gamma\text{-Fe}_2\text{O}_3/\text{b-TiO}_2$ heterojunctions has been established in Fig. 6. As shown in Fig. S8, the relative positions of valence-band maxima of b-TiO_2 (2.58 eV) and $\gamma\text{-Fe}_2\text{O}_3$ (0.95 eV) after hydrogenation, respectively. The VB of $\gamma\text{-Fe}_2\text{O}_3$ is lower than that of black TiO_2 , which promotes the photogenerated holes transferring to the valence band of black TiO_2 . The optical band gaps of black TiO_2 and $\gamma\text{-Fe}_2\text{O}_3$ after hydrogenation are ~ 3.07 and ~ 1.94 eV as shown in Fig. S9, respectively. The average optical band gap of $\alpha\text{-Fe}_2\text{O}_3/\text{b-TiO}_2$ and $\gamma\text{-Fe}_2\text{O}_3/\text{b-TiO}_2$ heterojunctions can be seen from the Fig. S10. The intermediate states, oxygen vacancies and Ti^{3+} are formed between conduction-band minimum (CB) and VBM of TiO_2 and Fe_2O_3 after hydrogenation, which can narrow band gap to facilitate the absorption of light and the separation of photogenerated electrons and holes. In this process of photocatalytic degradation of tetracycline, hydroxyl radicals ($\cdot\text{OH}$), superoxide anion ($\cdot\text{O}_2^-$) and H_2O_2 (Fig. S11) are the substances that play an important role in the oxidation. Testing methods for superoxide anion and hydrogen peroxide are discussed in detail in supporting information. As can be seen from Fig. 6, the electrons and holes of $\gamma\text{-Fe}_2\text{O}_3$ can be separated efficiently under AM 1.5 irradiation, in which the electrons are transferred to the CB, leaving the holes on the VB. Generally, these photo-generated electrons and holes would quickly recombine and only a spot of charges could take part in the photocatalytic reaction. Significantly, the successful construction of heterojunction after combining TiO_2 , a large number of the photo-generated electrons on the CB of TiO_2 tend to transfer to the Fe_2O_3 , consequently, the electrons on the Fe_2O_3 readily combine with adsorbed oxygen of the surface of the material and oxygen in the solution to form $\cdot\text{O}_2^-$, which is a strong oxidizing agent to degrade tetracycline. While the holes on the VB of b-TiO_2 would directly react with water or hydroxide ions, producing $\cdot\text{OH}$ with strong oxidation ability, resulting in efficient electron-hole pairs separation and enhancing efficiency of photocatalytic degradation.

In order to deeply identify the proposed degradation process of tetracycline, LC–MS techniques were used for qualitative analysis according to the mass spectrum. The detailed specific LC–MS analysis was shown in Table S2. During the whole degradation process, there are four main oxidizing active species, hydroxyl radicals ($\cdot\text{OH}$), hole (h^+), superoxide anion ($\cdot\text{O}_2^-$) and hydrogen peroxide (H_2O_2) after irradiation. According to mass spectrogram, the main thirteen products of m/z were namely 525, 496, 451, 367, 351, 461, 477, 417, 400, 353, 233, 183, 255. In the tetracycline molecules double bond, phenolic group and amine group are relatively high functional groups with relatively high electron density and easily attacked by radicals in photocatalytic oxidation [49]. During hydroxylation, a hydroxyl group attacks different positions of tetracycline molecules, forming three possible structures of $m/z = 461$, and then the hydroxyl continue to attacks the different positions of tetracycline molecules, forming a possible structure of $m/z = 477$ were displayed in the light blue box of the picture, coinciding with previous reports [50,51]. In addition, some small m/z can be seen in the mass spectrum, mainly result from the *N*-demethylation process indicated by the h^+ attack. Because of the lower *N*–C bond energy, the h^+ attack will promote the formation of the *N*-demethylation process to form a m/z 417 substance, and the holes further attack the high energy groups in the molecule and appear $m/z = 400$,

353, respectively [52]. The molecules of $m/z = 353$ were decomposed into $m/z = 183$ and 233, under the combined action of holes, hydroxyl groups and superoxide anion as can be seen from the red box of Scheme 1. In the process of photocatalytic degradation, superoxide anion and hydrogen peroxide were also detected, and some substances with larger molecular weight, such as m/z of 525, 496, 451 can be seen in the mass spectrogram. The possible degradation mechanism is that the superoxide anion and the hydrogen peroxide attack benzene ring and make the benzene ring open to generate $m/z = 525$, and then continue to oxidize the *N*-demethylation process to produce the molecule of $m/z = 496$, and then further oxidize the $\text{C}(\text{O})\text{NH}_2$ group and produce the ketone ($m/z = 451$). Subsequently, the key downstream intermediate with $m/z = 367$ may be formed upon oxidation of double bond of intermediate ($m/z = 451$). Finally, they are all converted to ketonea with small molecular weight ($m/z = 351$) [53]. The possible photocatalytic degradation process is shown in the green box of Scheme 1. All intermediates are non-toxic and do not cause two pollution. In the end all of the intermediates were oxidized to carboxylic acids ($m/z = 255$), and then completely decomposed to CO_2 and H_2O .

4. Conclusions

In summary, we have demonstrated the facile fabrication of defects-engineering of magnetic $\gamma\text{-Fe}_2\text{O}_3$ ultrathin nanosheets/mesoporous black TiO_2 hollow sphere heterojunctions with hollow structure by the metal-ion intervened hydrothermal technique and high temperature hydrogenation route under normal pressure. The excellent solar-driven photocatalytic performance of $\gamma\text{-Fe}_2\text{O}_3/\text{b-TiO}_2$ for degradation of highly biotoxic tetracycline implied the significant role of the introduction of $\gamma\text{-Fe}_2\text{O}_3$ nanosheets and the formation of heterojunction for improving the photocatalytic performance. Comparing $\gamma\text{-Fe}_2\text{O}_3/\text{b-TiO}_2$ with $\alpha\text{-Fe}_2\text{O}_3/\text{b-TiO}_2$, The apparent rate constant of the former photocatalytic degradation tetracycline is about 3 times higher than that of the latter under AM 1.5 and the $\cdot\text{OH}$ and electron density of the former was higher than that of the latter, which was ascribed to the formed Ti^{3+} in black TiO_2 frameworks and oxygen vacancy defects enhancing the solar-light-harvesting, and the ultrathin nanosheet and hollow structure favoring the separation and transportation of photogenerated charge carriers. In addition, magnetic separation was achieved due to the formation of $\gamma\text{-Fe}_2\text{O}_3$. Finally, we also used LC–MS to analyze the possible mechanism of photocatalytic oxidation. This facile strategy could potentially be applied as improving the photocatalytic performance of other existing semiconductor oxides for reducing energy consumption and cost in wastewater treatment.

Acknowledgments

We gratefully acknowledge the support of the National Natural Science Foundation of China (21631004, 51672073), and the University Nursing Program for Young Scholars with Creative Talents in Heilongjiang Province (UNPYSCT-2015014).

Appendix A. Supplementary data

Supplementary material related to this article can be found, in the online version, at doi:<https://doi.org/10.1016/j.apcatb.2018.08.033>.

References

- [1] X. Zheng, G. Shen, C. Wang, Y. Li, D. Dunphy, T. Hasan, C.J. Brinker, B.L. Su, *Nat. Commun.* 8 (2017) 14912.
- [2] Y. Xu, C. Zhang, P. Lu, X. Zhang, L. Zhang, J. Shi, *Nano Energy* 38 (2017) 494–503.
- [3] F. Brandl, N. Bertrand, E.M. Lima, R. Langer, *Nat. Commun.* 6 (2015) 7765.
- [4] H. Zhong, J. Zhang, X. Tang, W. Zhang, R. Jiang, R. Li, D. Chen, P. Wang, Z. Yuan, *Nat. Commun.* 8 (2017) 14525.
- [5] C. Wang, Y. Wu, J. Lu, J. Zhao, J. Cui, X. Wu, Y. Yan, P. Huo, *ACS Appl. Mater. Interfaces* 9 (2017) 23687–23697.

- [6] F. Chen, Q. Yang, X. Li, G. Zeng, D. Wang, C. Niu, J. Zhao, H. An, T. Xie, Y. Deng, *Appl. Catal. B: Environ.* 200 (2017) 330–342.
- [7] T. Lu, X. Xu, X. Liu, T. Sun, *Chem. Eng. J.* 308 (2017) 151–159.
- [8] W. Shi, F. Guo, H. Wang, M. Han, H. Li, S. Yuan, H. Huang, Y. Liu, Z. Kang, *Appl. Catal. B: Environ.* 219 (2017) 36–44.
- [9] L. Rimoldi, D. Meroni, G. Cappelletti, S. Ardizzzone, *Catal. Today* 281 (2017) 38–44.
- [10] F. Deng, L. Zhao, X. Luo, S. Luo, D.D. Dionysiou, *Chem. Eng. J.* 333 (2018) 423–433.
- [11] Y. Hong, C. Li, B. Yin, D. Li, Z. Zhang, B. Mao, W. Fan, W. Gu, W. Shi, *Chem. Eng. J.* 338 (2018) 137–146.
- [12] M. Ge, C. Cao, J. Huang, S. Li, Z. Chen, K.Q. Zhang, S.S. Al-Deyabd, Y. Lai, *J. Mater. Chem. A* 4 (2016) 6772–6801.
- [13] A. Sinhamahapatra, J.P. Jeon, J.-S. Yu, *J. Energy Environ. Sci.* 8 (2015) 3539–3544.
- [14] K. Zhang, L. Wang, J.K. Kim, M. Ma, G. Veerappan, C.L. Lee, K.J. Kong, H. Lee, J.H. Park, *Energy Environ. Sci.* 9 (2016) 499–503.
- [15] Y. Liu, H. Feng, X. Yan, J. Wang, H. Yang, Y. Du, W. Hao, *Dalton Trans.* 46 (2017) 10694–10699.
- [16] X. Zhang, J. Wang, W. Hu, K. Zhang, B. Sun, G. Tian, B. Jiang, K. Pan, W. Zhou, *ChemCatChem* 8 (2016) 3240–3246.
- [17] X. Chen, L. Liu, P.Y. Yu, S.S. Mao, *Science* 331 (2011) 746–750.
- [18] Z. Wang, C. Yang, T. Lin, H. Yin, P. Chen, D. Wan, F. Xu, F. Huang, J. Lin, X. Xie, M. Jiang, *Energy Environ. Sci.* 6 (2013) 3007–3014.
- [19] W. Zhou, W. Li, J.Q. Wang, Y. Qu, Y. Yang, Y. Xie, K. Zhang, L. Wang, H. Fu, D. Zhao, *J. Am. Chem. Soc.* 136 (2014) 9280–9283.
- [20] X. Chen, L. Liu, F. Huang, *Chem. Soc. Rev.* 44 (2015) 1861–1885.
- [21] X. Zhang, W. Hu, K. Zhang, J. Wang, B. Sun, H. Li, P. Qiao, L. Wang, W. Zhou, *ACS Sustain. Chem. Eng.* 5 (2017) 6894–6901.
- [22] D. Liu, Y. Liu, P. Huang, C. Zhu, Z. Kang, J. Shu, M. Chen, X. Zhu, J. Guo, L. Zhuge, X. Bu, P. Feng, T. Wu, *Angew. Chem. Int. Ed.* 57 (2018) 1–6.
- [23] J. Hou, H. Cheng, C. Yang, O. Takeda, H. Zhu, *Nano Energy* 18 (2015) 143–153.
- [24] S. Kment, F. Riboni, S. Pausova, L. Wang, L. Wang, H. Han, Z. Hubicka, J. Krysa, P. Schmuki, R. Zboril, *Chem. Soc. Rev.* 46 (2017) 3716–3769.
- [25] J.C. Wang, L. Zhang, W.X. Fang, J. Ren, Y.Y. Li, H.C. Yao, J.S. Wang, Z.J. Li, *ACS Appl. Mater. Interfaces* 7 (2015) 8631–8639.
- [26] Y. Jin, L. Dang, H. Zhang, C. Song, Q. Lu, F. Gao, *Chem. Eng. J.* 326 (2017) 292–297.
- [27] B.F.L. Formai, M. Grätzel, K. Sivula, *Adv. Funct. Mater.* 20 (2010) 1099–1107.
- [28] B. Sun, W. Zhou, H. Li, L. Ren, P. Qiao, F. Xiao, L. Wang, B. Jiang, H. Fu, *Appl. Catal. B: Environ.* 221 (2018) 235–242.
- [29] W. Hu, W. Zhou, K. Zhang, X. Zhang, L. Wang, B. Jiang, G. Tian, D. Zhao, H. Fu, *J. Mater. Chem. A* 4 (2016) 7495–7502.
- [30] J. Wang, H. Yu, X. Zhou, X. Liu, R. Zhang, Z. Lu, J. Zheng, L. Gu, K. Liu, D. Wang, L. Jiao, *Nat. Commun.* 8 (2017) 377.
- [31] W.H. Yang, C.F. Lee, H.Y. Tang, D.B. Shieh, C.S. Yeh, *J. Phys. Chem. B* 110 (2006) 14087–14091.
- [32] M. Wang, K. Deng, W. Lü, X. Deng, K. Li, Y. Shi, B. Ding, Z. Cheng, B. Xing, G. Han, Z. Hou, J. Lin, *Adv. Mater.* 30 (2018) 1706747.
- [33] K. Zhang, W. Zhou, X. Zhang, B. Sun, L. Wang, K. Pan, B. Jiang, G. Tian, H. Fu, *Appl. Catal. B: Environ.* 206 (2017) 336–343.
- [34] X. Pan, M.Q. Yang, X. Fu, N. Zhang, Y.J. Xu, *Nanoscale* 5 (2013) 3601–3614.
- [35] C. Li, T. Wang, Z.J. Zhao, W. Yang, J.F. Li, A. Li, Z. Yang, G.A. Ozin, J. Gong, *Angew. Chem. Int. Ed.* 57 (2018) 5278–5282.
- [36] J. Liu, S. Yang, W. Wu, Q. Tian, S. Cui, Z. Dai, F. Ren, X. Xiao, C. Jiang, *ACS Sustain. Chem. Eng.* 3 (2015) 2975–2984.
- [37] L. Sun, W. Wu, Q. Tian, M. Lei, J. Liu, X. Xiao, X. Zheng, F. Ren, C. Jiang, *ACS Sustain. Chem. Eng.* 4 (2016) 1521–1530.
- [38] D. Yang, A. Gulzar, G. Yang, S. Gai, F. He, Y. Dai, C. Zhong, P. Yang, *Small* 13 (2017) 1703007.
- [39] G. Zhu, T. Lin, X. Lu, W. Zhao, C. Yang, Z. Wang, H. Yin, Z. Liu, F. Huang, J. Lin, *J. Mater. Chem. A* 1 (2013) 9650–9653.
- [40] T. Yu, X. Cheng, X. Zhang, L. Sui, Y. Xu, S. Gao, H. Zhao, L. Huo, *J. Mater. Chem. A* 3 (2015) 11991–11999.
- [41] S. Gao, Z. Sun, W. Liu, X. Jiao, X. Zu, Q. Hu, Y. Sun, T. Yao, W. Zhang, S. Wei, Y. Xie, *Nat. Commun.* 8 (2017) 14503.
- [42] X. Pan, M.Q. Yang, X. Fu, N. Zhang, Y.J. Xu, *Nanoscale* 5 (2013) 3601–3614.
- [43] Y. Yang, L.C. Yin, Y. Gong, P. Niu, J.Q. Wang, L. Gu, X. Chen, G. Liu, L. Wang, H.M. Cheng, *Adv. Mater.* 30 (2018) 1704479.
- [44] H. Li, L. Shen, K. Zhang, B. Sun, L. Ren, P. Qiao, K. Pan, L. Wang, W. Zhou, *Appl. Catal. B: Environ.* 220 (2018) 111–117.
- [45] H. Xu, Y. Jiang, X. Yang, F. Li, A. Li, Y. Liu, J. Zhang, Z. Zhou, L. Ni, *Mater. Res. Bull.* 97 (2018) 158–168.
- [46] X. Wang, M. Hong, F. Zhang, Z. Zhuang, Y. Yu, *ACS Sustain. Chem. Eng.* 4 (2016) 4055–4063.
- [47] X. Jia, R. Dai, D. Lian, S. Han, X. Wu, H. Song, *Appl. Surf. Sci.* 392 (2017) 268–276.
- [48] C. Mao, F. Zuo, Y. Hou, X. Bu, P. Feng, *Angew. Chem. Int. Ed.* 126 (2014) 10653–10657.
- [49] J. Wang, D. Zhi, H. Zhou, X. He, D. Zhang, *Water Res.* 137 (2018) 324–334.
- [50] Y. Ji, Y. Shi, W. Dong, X. Wen, M. Jiang, J. Lu, *Chem. Eng. J.* 298 (2016) 225–233.
- [51] Y. Yang, Z. Zeng, C. Zhang, D. Huang, G. Zeng, R. Xiao, C. Lai, C. Zhou, H. Guo, W. Xue, M. Cheng, W. Wang, J. Wang, *Chem. Eng. J.* 349 (2018) 808–821.
- [52] G. Dong, L. Huang, X. Wu, C. Wang, Y. Liu, G. Liu, L. Wang, X. Liu, H. Xia, *Chemosphere* 193 (2018) 702–710.
- [53] Z. Xie, Y. Feng, F. Wang, D. Chen, Q. Zhang, Y. Zeng, W. Lv, G. Liu, *Appl. Catal. B: Environ.* 229 (2018) 96–104.